Article:
Quirk, James A., Lazarov, Vlado K. orcid.org/0000-0002-4314-6865 and Mckenna, Keith P. orcid.org/0000-0003-0975-3626 (2020) First-Principles Modeling of Oxygen-Deficient Anatase TiO2Nanoparticles. Journal of Physical Chemistry C. 23637–23647. ISSN: 1932-7455

https://doi.org/10.1021/acs.jpcc.0c06052

THE JOURNAL OF PHYSICAL CHEMISTRY C

pubs.acs.org/JPCC Article

First-Principles Modeling of Oxygen-Deficient Anatase TiO_2 Nanoparticles

James. A. Quirk,* Vlado K. Lazarov, and Keith P. McKenna

Cite This: *J. Phys. Chem. C* 2020, 124, 23637−23647

Read Online

ACCESS | Metrics & More | Article Recommendations

ABSTRACT: First-principles calculations of the electronic structure of reduced anatase TiO_2 nanoparticles are performed using a hybrid density functional theory approach for an accurate description of charge trapping. It is found that, in the bulk and at extended surfaces, electrons introduced by oxygen vacancies delocalize but, in reduced nanoparticles, electrons preferentially localize (forming Ti^{3+} species) at low-coordinated sites on the surface of the particle. It is favorable for nanoparticles to be oxygen-deficient in oxygen-poor conditions with the $Ti_{33}O_{66}$ nanoparticle being significantly easier to reduce than the larger $Ti_{151}O_{302}$ nanoparticle. Since low-coordinated sites are more prevalent in smaller nanoparticles, this suggests that there is a delicate balance between the number of carriers introduced by vacancies and the number of trapped electrons.

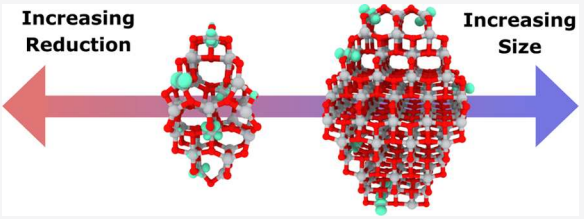

INTRODUCTION

Titanium dioxide (TiO_2) is an abundant and inexpensive semiconductor material that enjoys a wide range of environmental and energy-production applications including the following: as a photocatalyst, where it can be used to split water for hydrogen production[1−4] or to break down pollutants for wastewater remediation;[5−7] as an electron transport medium in dye-sensitized and perovskite solar cells;[8−10] and as an anode material for rechargeable batteries, where it allows intercalation of ions such as lithium or sodium.[11−16] To engineer suitable properties for these applications, it is important to understand the behavior of charge carriers in the material. Charge carriers can be introduced into a system by photoexcitation, by doping, or by injection from another medium. Once introduced, charge carriers can become trapped at point defects (such as vacancies and impurities) or extended defects (such as surfaces and grain boundaries), or in the pristine lattice (where the charge carrier creates a local polarization and becomes self-trapped as a small polaron).[17−22] Charge trapping can be beneficial, such as in the case of a carrier trapped at a surface being able to interact with adsorbates in catalytic applications,[23,24] or it can be detrimental as trapping will lead to lower charge mobility and can lead to increased rates of recombination, which will reduce open-circuit voltage and the efficiency of photovoltaic and battery devices.

TiO_2 has many polymorphs with two of the most common being rutile and anatase. Of these two, anatase shows greater promise due to having higher electron mobility and photocatalytic activity when compared to rutile. However, anatase is not thermodynamically stable as large, single crystals, so usually sol−gel synthesis is used to produce nanoparticles that can then be sintered together, resulting in highly defective samples.[25,26] Electron paramagnetic resonance (EPR) studies indicate that anatase will readily trap holes on oxygen ions (forming O^- species) but will only trap a comparatively small number of electrons (as Ti^{3+} species),[27] but the exact nature of these electron traps is not fully understood. In contrast, rutile exhibits large numbers of trapped electrons but a relatively small number of trapped holes, accounting for the low electron mobility of rutile in comparison to anatase.[28,29] Due to the polycrystalline nature of these samples, it is extremely challenging to confidently collect and interpret experimental results. This drives a need for first-principles calculations to provide insight at the atomic scale, but that is not to suggest that computational work is not fraught with its own challenges regarding the confident interpretation of results.

Density functional theory (DFT) has become the de facto standard of electronic structure theory due to its low computational cost and reasonable accuracy, assuming that a suitable functional has been chosen to approximate the exchange−correlation energy. Generally, these functionals will be local or semilocal approximations, with a common example being the much-used Perdew−Burke−Ernzerhof (PBE) functional,[30] which is relatively robust and performs well for a variety of properties.[31,32] However, the PBE

Received: July 2, 2020
Revised: September 30, 2020
Published: October 15, 2020

https://dx.doi.org/10.1021/acs.jpcc.0c06052
J. Phys. Chem. C 2020, 124, 23637−23647

approximation is, like all DFT functionals, plagued by the self-interaction error (SIE) whereby an electron spuriously interacts with its own density. The SIE has a tendency toward artificially stabilizing delocalized states,[33] making semilocal DFT a poor choice where there is a desire to make predictions regarding charge localization and trapping. Frequently, when attempting to correct for the SIE, hybrid DFT is employed, which incorporates desirable features of the Hartree−Fock theory by mixing in some fraction of the nonlocal Fock exchange into the usual semilocal approximations.[34] Hybrid DFT is far more computationally demanding than standard DFT due to calculation of the Fock exchange term but, as hardware improves and new time-saving methods are implemented, hybrid DFT is becoming feasible for large systems containing hundreds of atoms. With the roadblock of computational cost being gradually removed, the pressing question still remains: What fraction of Fock exchange should one include in a hybrid functional?

A straightforward example of how a hybrid functional might be parameterized is where the hybrid exchange energy, E_x^{hyb}, takes the form of a simple linear combination

$$E_x^{hyb} = \alpha E_x^{HF} + (1 - \alpha)E_x^{PBE} \quad (1)$$

where E_x^{HF} is the Fock exchange energy, E_x^{PBE} is the exchange component of the PBE energy functional, and α is the fraction of the Fock exchange to be mixed in. This is the form taken by the PBE0 functional, where the Görling−Levy perturbation theory is used to show that a value of $\alpha = 0.25$ should be appropriate to describe ionization and atomization energies in many systems.[35,36] However, it must be remembered that neither semilocal DFT nor Hartree−Fock is an exact theory, so there must be no expectation that a simple linear combination of both theories can be applied universally. Instead, a specific value of α may be necessary for a given material as, if the value of α is too low, then an insufficient amount of SIE will be removed and localized states will not be sufficiently stabilized or, if the value of α is too high, then localized states will become erroneously stable and incorrect predictions may be made. Too high a fraction of Fock exchange also runs the risk of losing some of the desirable features of DFT as, while the inclusion of Fock exchange might do well in removing the SIE, it can also introduce potentially dominating amounts of static correlation error that are usually comparatively small in standard DFT approximations.[37] Taking the same linear form of PBE0 and tuning α in a case-by-case manner leads to a class of hybrid functionals that shall be referred to in this work as PBEα to distinguish them from the unique case of PBE0.

When constructing a PBEα functional, it is possible to take an empirical approach by tuning a value of α that reproduces experimental features, commonly the band gap. Such empirical functionals are commonplace and often produce results in good agreement with the experiment.[38−40] Empirical functionals do, however, come with limitations in their predictive power due to the fact that they rely on prior knowledge of accurate experimental values, which may not be known when studying lesser-known or experimentally problematic materials. A relevant example would be brookite, another phase of TiO_2, where experimental values for the band gap vary between 3.1 and 3.4 eV.[41] Empirical functionals have a trade-off in terms of universality as there is no real reason to expect that an approximate hybrid functional that gives the correct band gap would also give all other properties of interest correctly. For example, it is observed that functionals tuned to the band gap can still incorrectly predict photoluminescent peaks.[42] Some nonempirical approaches aim to tune α to grant some desirable features to the PBEα functional. For example, the so-called dielectric-dependent hybrid recognizes that hybrid DFT is effectively a further, frequency-independent approximation to the Coulomb hole and screened exchange (COHSEX) approximation to the GW self-energy. It can then be shown that $\alpha = \epsilon^{-1}$ (where ϵ is the dielectric constant) reasonably approximates the COHSEX approximation. Dielectric-dependent hybrids generally yield good band gaps and are thought that they should provide good inputs for G_0W_0 calculations.[43,44] This approach is not, however, based on some fundamental property of the exact functional but is instead attempting to use hybrid DFT to approximate a higher-order method. Another approach is to construct a hybrid functional that best reproduces a known property of the exact functional. The choice of constraint can be made based on which constraint is most important to satisfy when studying a particular quantity of interest.

One such property that the exact functional must satisfy is the generalized Koopmans' condition (GKC), which gives an expression for the ionization energy of a system of an N electron, $I(N)$, as

$$-I(N) \equiv E(N) - E(N - 1) = \epsilon_N(N) \quad (2)$$

where $E(N)$ is the total energy of an N electron system, and $\epsilon_i(N)$ is the ith eigenvalue of the N electron system. Hybrid functionals that have been tuned to satisfy the GKC have been shown to accurately reproduce experimental results for molecular systems[45−47] as well as yielding accurate electron densities in simple model systems where the exact density is known.[48] One drawback is that the GKC is not as applicable to delocalized states, such as band edges in a periodic solid, due to an idiosyncrasy of periodic calculations, which can lead to difficult tuning to the GKC for solid materials.[49] However, in the case of titanium dioxide, the presence of self-trapped polarons provides a convenient localized state against which a functional can be tuned to GKC in the bulk lattice. Previous work in our group constructed GKC-tuned functionals based on polarons in the bulk of various phases of TiO_2. We use a modification of PBEα, which utilizes the same linear mixing as PBEα but truncates the Fock exchange contribution at long ranges to reduce the computational cost for large systems.[50] It was found that the optimum value to satisfy the GKC in bulk anatase is $\alpha = 0.105$.[51] Aside from performing well for charge trapping in the bulk, this value of α also shows good results for the band gap, yielding 2.94 eV compared to the experimental value of 3.2 eV, only an 8% error. Furthermore, $\alpha = 0.105$ predicts that, at zero temperature, rutile is slightly less stable than anatase by 0.092 eV unit^{-1}, which is in good agreement with very high-quality quantum Monte Carlo simulations, which predict that rutile is less stable by 0.041 eV unit^{-1}.[52]

Using this GKC-tuned functional, it is predicted that hole polarons can form in bulk anatase but not electron polarons (in agreement with the higher proportion of observed hole traps in EPR),[53] but evidence of trapped electrons in anatase remains elusive. Using the same functional, a study of extended surfaces predicted that high-index surfaces of anatase would be able to trap electrons on undercoordinated Ti sites but that the low-index facets present in equilibrium crystals show no electron-trapping behavior[54] and a study of low formation energy twin boundaries also yielded no evidence of electron trapping.[55]

https://dx.doi.org/10.1021/acs.jpcc.0c06052
J. Phys. Chem. C 2020, 124, 23637−23647

Point defects must also be considered, with the most common and technologically relevant being the oxygen vacancy. A missing oxygen will introduce two excess electrons into the lattice, but calculations using the GKC-tuned approach have shown that the lowest-energy configuration taken by a neutral oxygen vacancy is one where both excess electrons are delocalized throughout the bulk. This delocalized solution is around 0.95 eV lower in energy than a solution where both electrons are localized and 0.47 eV lower in energy than a solution where one electron is localized.[56] Such a result should not be especially surprising as, if it were always favorable for electrons to become strongly trapped in the vicinity of vacancies, then vacancies would not be able to effectively dope anatase to become n-type.

All of the theoretical studies described so far are concerned with high-symmetry, extended systems but such systems will not capture certain features of nanoparticles. For example, even a perfect equilibrium nanoparticle made up of pristine surfaces will contain edges and vertices where facets meet. Such features have low symmetry and would not be trivial to model in a periodic supercell. The examples of first-principles modeling of nanoparticles that do exist are often limited in their scope or applicability. Many studies perform all calculations using local or semilocal DFT.[57,58] Another approach is to optimize the geometry using semilocal functionals and then apply a hybrid density functional to a fixed geometry.[59,60] This is an improved approach but it is not, however, without issues when describing localized charges. Small polaronic states and their associated geometric distortion to the crystal lattice are inseparably linked; if a functional cannot properly describe localized charges, it cannot properly describe the geometry that would allow the charge to become localized. Nevertheless, it can still provide valuable insight into situations where charge localization is not as relevant. For example, such an approach has been used to determine that the properties of an anatase nanoparticle start to linearly approach bulk-like behavior at sizes beyond roughly 3 nm (beyond around 200 atoms), providing a valuable benchmark when constructing model nanoparticles.[61] Other studies have been carried out where geometries of anatase nanoparticles have been determined through a global optimization procedure where energies are determined using hybrid DFT,[62,63] which should be expected to provide more accurate descriptions of energetics and electronic structure, but only consider stoichiometric particles.providing more reasonable results than A previous study examined the properties of a single oxygen vacancy on a $Ti_{84}O_{168}$ nanoparticle using hybrid density functional theory using both standard PBE0 and a parameterization of PBEα using α = 0.125, similar to our GKC-tuned value of α = 0.105.[64,65] This study shows that the choice of α has pronounced effects on the specific location and spin configuration of the most stable vacancy, with the value of α = 0.125 providing more reasonable results than PBE0. Reassuringly, it seems that qualitative trends, and therefore the associated predictions that can be made from them, are less affected by the choice of functional. Results from single oxygen vacancies are extremely useful but, in reality, nanoparticles should probably be expected to have multiple oxygen vacancies, though the rough amount of vacancies to be expected and how they interact is unclear. A natural next step would be to determine the degree to which nanoparticles can be reduced and what properties these highly reduced particles would have.

Here, we present hybrid DFT calculations of the atomic and electronic structures of explicit models of $Ti_{33}O_{66}$ and $Ti_{151}O_{302}$ anatase nanoparticles, where all calculations, including geometry optimizations, are carried out using a hybrid density functional that has been shown to effectively remove the self-interaction error in bulk anatase. We consider the reduction of these particles by the formation of oxygen vacancies to determine the behavior of excess charge in the nanoparticles. We also consider the facets appearing in the Wulff construction of anatase, the {101} facets, the {001} facets, and the possible reconstruction of the {001} facet, and determine the position of the most stable vacancy in the vicinity of these surfaces. It is shown that excess electrons introduced by vacancies in the vicinity of extended surfaces preferentially delocalize but the excess electrons in nanoparticles prefer to localize on undercoordinated Ti sites.

THEORETICAL METHODS

All electronic structure calculations were carried out using hybrid DFT, where some fraction of the Hartree−Fock (HF) exchange is mixed into the Perdew−Burke−Ernzerhof (PBE) functional[30] to correct the self-interaction error present in standard semilocal approximations for exchange−correlation.[66−68] We use the implementation of hybrid DFT within CP2K,[69] where we use a truncated HF exchange functional (which we term PBEα-TC-LRC)[50,70] in which, beyond some cutoff radius, PBE exchange is used instead of HF exchange. We determine that a cutoff radius of 6 Å is well converged with regard to lattice parameter and band gap. A further measure to reduce computational cost is the augmented density matrix method (ADMM)[71] in which exchange integrals are approximated through mapping onto smaller, more localized basis sets. For both Ti and O, we use triple-ζ basis sets optimized from molecular calculations (MOLOPT)[72] and Goedecker−Teter−Hutter pseudopotentials available within CP2K.[73−75] We mix in 10.5% HF exchange, a fraction that ensures that the generalized Koopmans' condition is obeyed to within 0.05 eV in bulk anatase.[51,54] This GKC-tuned functional is found to be in good agreement with the experiment with regard to polaron formation.[48,51] We use five multigrids with a relative cutoff of 60 Ry and the finest grid having a cutoff of 600 Ry. As CP2K only samples the Γ-point, we converge properties with respect to the supercell size as opposed to the k-point sampling in reciprocal space. A 5 × 5 × 2 expansion of the conventional anatase unit cell is sufficient to yield lattice parameters of $a = b$ = 3.78 Å and c = 9.61 Å, which are within 1% of experimentally determined parameters. A more detailed description of the parameterization of this functional for anatase, and other TiO_2 polymorphs, as well as corresponding convergence testing, can be found in our previous work.[51]

The surfaces are modeled as slabs in a periodic supercell where slabs are over 24 Å thick, with surface areas between 200 and 300 Å^2 and a vacuum gap of at least 12 Å. The surface models used in this work are taken from a previous study where analysis and discussion of convergence with respect to slab thickness are given.[54] For the {001} and {101}, seven atomic layers were considered to be in the vicinity of the surface. For the reconstructed {001}, all symmetrically inequivalent sites across five atomic layers were considered to be in the vicinity of the surface. Oxygen vacancies were modeled using a ghost basis placed in the position of the vacant oxygen. All geometry optimization performed on

https://dx.doi.org/10.1021/acs.jpcc.0c06052
J. Phys. Chem. C 2020, 124, 23637−23647

extended surfaces is performed until the force on ions is less than 0.01 eV $Å^{-1}$.

The procedure to determine stable configurations for reduced nanoparticles first required the construction of $Ti_{33}O_{66}$ and $Ti_{151}O_{302}$ models where the shapes were based on the Wulff construction, using the surface energies for the {101} and {001}. Then, a large number of starting structures were generated by randomly removing oxygen from the particle. These structures were then sorted by the total coordination number to remove the particles with the lowest number of bonds, assuming that these systems will be less favorable. This is an educated assumption supported by a previous study that shows that lower-coordinated oxygen is, in general, easier to remove from nanoparticles.[64] A selection of configurations were chosen such that each stoichiometry explored systems containing surface vacancies, subsurface vacancies, and a mixture of both. In total, there were three configurations explored for each stoichiometry and the lowest-energy system for each stoichiometry was taken forward for analysis. For the $Ti_{33}O_{33(2-\delta)}$ particle, we generated a series of stoichiometries by removing 1 O at a time up to 8 removed O (δ = 0.24) and for the $Ti_{151}O_{151(2-\delta)}$ we generated a series of stoichiometries by removing 2 O at a time up to 12 removed O (δ = 0.07). For the large particle approximations, the facet surface areas and volumes of Wulff constructions, and hence the number of O sites of a given kind, were determined using WulffPack.[76] Nanoparticles were modeled in an aperiodic cell using the Martyna−Tuckerman Poisson solver,[77] where the simulation cells for each particle are made to be over twice the size of the charge density. All geometry optimization on nanoparticles is performed until the force on ions is less than 0.1 eV $Å^{-1}$.

For all calculations, the number of electrons in each spin channel is kept equal, such that there is no net magnetization in the system. This compromise primarily serves to reduce the size of spin configuration space for the nanoparticle calculations. While a true global minimum may be a system with some net magnetization, the energy contribution due to the spin configurations is expected to be small compared to other contributions from charge localization and the position of the vacancy. This is supported by calculations in bulk anatase where the difference between the singlet and triplet configurations of an oxygen vacancy with two localized electrons is only 0.09 eV. This energy difference is an order of magnitude smaller than the 0.95 eV energy difference between the localized singlet solution and the solution where two electrons are delocalized across the simulation cell.[56]

RESULTS AND DISCUSSION

Oxygen Vacancies at Surfaces. First, to investigate the properties of large nanoparticles that are oxygen-deficient, we consider O vacancies in the vicinity of the facets appearing in the Wulff construction of anatase: the {101} facets and {001} facets, with the {001} facet having a possible reconstruction. In this reconstruction, bridging O sites along the surface are periodically replaced with units of TiO_3, which acts to relieve strain and lowers the surface energy to about half that of the clean, unreconstructed {001} surface.[78,79] This reconstruction is, however, typically observed in thin-film samples annealed in vacuum, and it is unclear how large the drive to reconstruct would be in other situations. For example, in the case of a small particle, the space available for a reconstruction is limited and it would also be possible to relieve strain through relaxation of the entire particle. The surface formation energy, γ, is defined as

$$\gamma = \frac{E_{slab} - NE_{bulk}}{2A} \tag{3}$$

where E_{slab} is the total energy of the surface slab model, N is the number of units of anatase in the slab, E_{bulk} is the energy of one unit of bulk anatase, and A is the area of the surface where the factor of 2 accounts for there being two surfaces in the periodic slab. The {101}, {001}, and reconstructed {001} facets are calculated to have $\gamma_{\{101\}}$ = 0.46 J m^{-2}, $\gamma_{\{001\}}$ = 0.99 J m^{-2}, and $\gamma^{recon.}_{\{001\}}$ = 0.59 J m^{-2}, respectively.

We focus on the most stable vacancy in the vicinity of each surface where the formation energy of an O vacancy at a surface, $E_F^{vacancy}$, is defined as

$$E_F^{vacancy} = E_{slab}^{vacancy} - E_{slab} + \mu_O \tag{4}$$

where $E_{slab}^{vacancy}$ is the energy of the surface slab containing the vacancy, E_{slab} is the energy of the pristine surface slab, and μ_O is the O chemical potential. The value of μ_O in O-rich conditions is taken to be

$$\mu_O = \frac{1}{2}E_{O_2} \tag{5}$$

where E_{O_2} is the total energy of an oxygen molecule in the gas phase. Then, we can define the chemical potential of Ti, μ_{Ti}, as

$$\mu_{Ti} = E_{TiO_2} - E_{O_2} \tag{6}$$

For O-poor conditions, we choose the chemical potentials corresponding to anatase in equilibrium with corundum (TiO_2/Ti_2O_3)

$$\mu_{Ti} + 2\mu_O = E_{TiO_2} \tag{7a}$$

$$2\mu_{Ti} + 3\mu_O = E_{Ti_2O_3} \tag{7b}$$

where $E_{Ti_2O_3}$ is the energy of a unit of bulk corundum. Going from O-rich to O-poor corresponds to a shift in the chemical potential of $\Delta\mu_O$ = −3.96 eV. The rationale for choosing Ti_2O_3 instead of TiO or metallic Ti is that Ti_2O_3 is the more stable material over a wide range of μ_O, which suggests that considering the equilibrium with Ti_2O_3 provides the most meaningful limit on the TiO_2 growth.[18,56,80,81]

For the {001} and reconstructed {001} surfaces, the most stable vacancy occurs at the surface, whereas in the {101}, the most stable vacancy occurs at a subsurface site (Figure 1). The subsurface vacancy in the {101} is found to have a comparable formation energy to a vacancy in the bulk, only 0.04 eV more favorable. This is consistent with the evidence that vacancies have a tendency to segregate away from the {101} to the subsurface and bulk even at low temperatures.[82,83] For O vacancies at both the {001} and reconstructed {001} surfaces, we find that it is significantly more favorable to form vacancies, with formation energies 1.44 and 0.80 eV lower than the bulk-like solution, respectively. It is predicted that vacancies would be favorable to form in the O-poor limit (Figure 2). However, it is important to note that the vacancy formation energies were calculated for relatively dilute vacancies in a supercell and that the negative formation energies in the oxygen-poor limit should not be taken to imply that all surface sites would be removed, nor would it provide an accurate approximation of the concentration of vacancies at these surfaces in such a limit.

https://dx.doi.org/10.1021/acs.jpcc.0c06052
J. Phys. Chem. C 2020, 124, 23637−23647

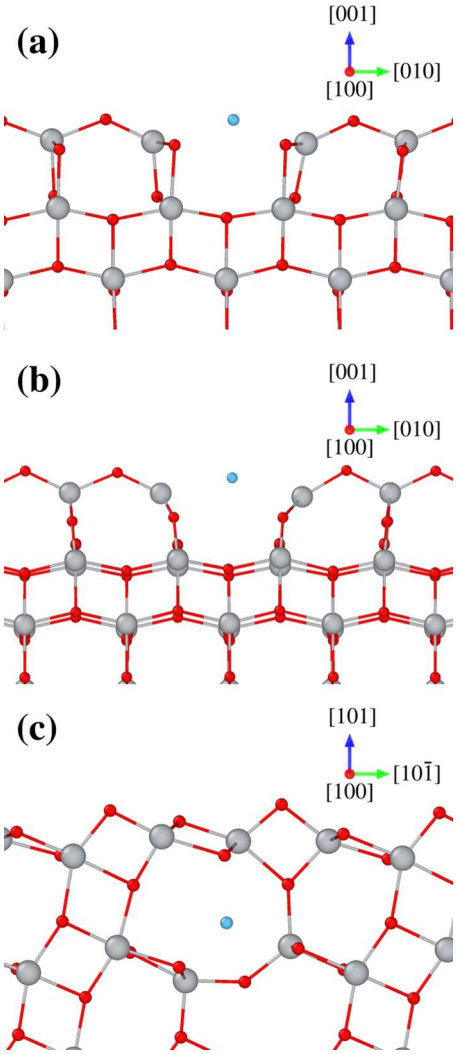

Figure 1. Structures of the most stable vacancies at the (a) unreconstructed {001} surface, (b) {001} reconstructed surface, and (c) {101} surface. Titanium and oxygen ions are represented by gray and red spheres, respectively. The blue spheres indicate the position of the vacant oxygen.

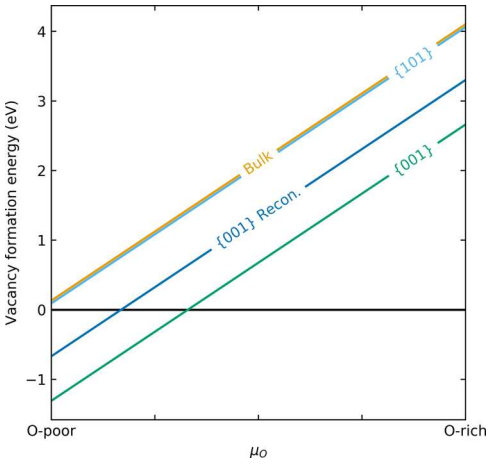

Figure 2. Formation energies of the most stable neutral vacancies in bulk and in the vicinity of the majority facets of anatase as a function of the oxygen chemical potential, μ_O. The {101} and bulk formation energies are comparable.

Similar to the O vacancy in the bulk anatase, the excess electrons prefer to delocalize in all of the considered vacancies near surfaces. These delocalized configurations come with a large distortion to the underlying lattice as ions move to screen the effect of the missing oxygen. From these results, we conclude that dilute oxygen vacancies in extended surfaces would not be likely to present trapped charges detectable by EPR. Also of note is that the introduction of lower-coordinated Ti species into the majority surfaces does not lead to electron trapping as was observed in a recent study of high-index facets.[54]

Reduced Nanoparticles. Low-energy configurations for a $Ti_{33}O_{33(2-\delta)}$ nanoparticle (diameter, $d \approx 1.5$ nm; Figure 3a) and a $Ti_{151}O_{151(2-\delta)}$ nanoparticle ($d \approx 2.5$ nm; Figure 3b) were determined as described in the Theoretical Methods section. For the $Ti_{33}O_{33(2-\delta)}$ nanoparticles, we consider values of δ = 0.00−0.24 and for the $Ti_{151}O_{151(2-\delta)}$ we consider δ = 0.00−0.07. For an explicit model of a nanoparticle of stoichiometry $Ti_NO_{N(2-\delta)}$, we calculate the formation energy, $E_F^{particle}$, as

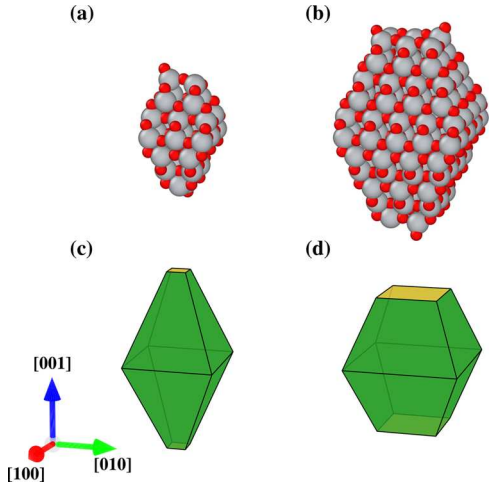

Figure 3. Models of (a) atomic structure of $Ti_{33}O_{66}$ nanoparticle, (b) atomic structure of $Ti_{151}O_{302}$ nanoparticle, (c) Wulff construction involving {101} and {001} facets, and (d) Wulff construction involving {101} and reconstructed {001} facets. Titanium and oxygen ions are represented by gray and red spheres, respectively. {101} and {001} facets are represented by green and yellow facets, respectively.

$$E_F^{particle} = E_{particle} - NE_{TiO_2} - \delta N\mu_O \quad (8)$$

where $E_{particle}$ is the total energy of the particle and E_{TiO_2} is the energy of a unit of bulk anatase. For a "macroscopic" particle of stoichiometry $Ti_NO_{N(2-\delta)}$, we calculate the formation energy E_F^{macro} as

$$E_F^{macro} = \sum_i (A_i\lambda_i - \delta N_i^O E_{F,i}^{vacancy}) - \delta N_{bulk}^O E_{F,bulk}^{vacancy} \quad (9)$$

where A_i is the area of the ith facet, λ_i is the surface formation energy of the ith facet, N_i^O is the number of stable O vacancy locations on the ith facet, N_{bulk}^O is the number of bulk-like O sites not considered as being part of the surface, and $E_{F,bulk}^{vacancy}$ is the formation energy of an O vacancy in bulk. For a nanoparticle containing {101} facets and {001} facets, the Wulff construction consists of 98.3% {101} facets and 1.7% {001} facets (Figure 3c), and for a nanoparticle containing {101} facets and reconstructed {001} facets, the Wulff

https://dx.doi.org/10.1021/acs.jpcc.0c06052
J. Phys. Chem. C 2020, 124, 23637−23647

construction consists of 87.5% {101} facets and 12.5% reconstructed {001} (Figure 3d). These calculations are performed at zero temperature where we do not consider the effects of entropy.

In the O-rich limit, we observe that stoichiometric particles are always more favorable than their reduced counterparts. However, in the O-poor limit, it is favorable to remove O from the particles, with the smaller particle being easier to reduce than the larger particle (Figure 4). In the O-poor limit, the

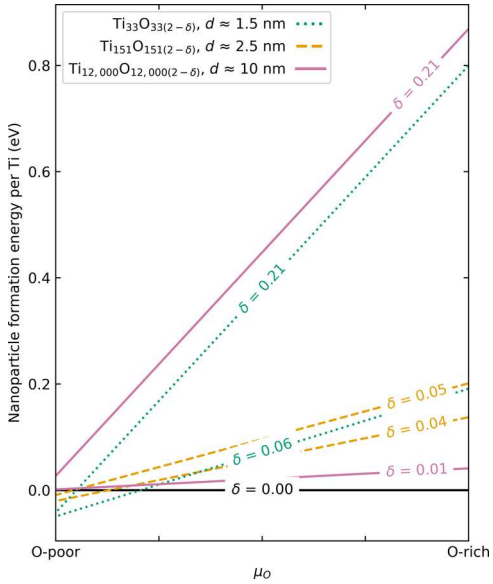

Figure 4. Formation energies per Ti atom plotted as a function of μ_O for $Ti_{33}O_{33(2-\delta)}$, $Ti_{151}O_{151(2-\delta)}$, and the macroscopic $Ti_{12\,000}O_{12\,000(2-\delta)}$ nanoparticles for various values of δ. All formation energies are taken relative to the stoichiometric configuration (δ = 0.00) of the corresponding size of nanoparticles.

most reduced particles with a favorable formation energy were $Ti_{33}O_{59}$ (δ = 0.21, for the small particle) and $Ti_{151}O_{294}$ (δ = 0.05, for the large particle). The calculated formation energies per Ti for macroscopic particles exhibit low dependence on the size of the particle, and so, for illustrative purposes, we choose an example case of a $Ti_{12\,000}O_{12\,000(2-\delta)}$ nanoparticle ($d \approx 10$ nm, around what would be observed in the experiment, consisting of 326.35 nm^2 {101} facets and 5.54 nm^2 {001} facets), using comparable values of δ, where we have assumed that vacancies are spread homogeneously throughout bulk and surface sites (Figure 4). Due to the form of eq 9, the formation energy per Ti varies little with the size of the particle, so we show only the $Ti_{12\,000}O_{12\,000(2-\delta)}$ example. It is clear that larger particles are not as readily reducible to the same degree as smaller particles. One factor responsible for this is the presence of low-symmetry and low-coordinated sites. For example, to make a nanoparticle stoichiometric without the presence of O interstitials or Ti vacancies, it is necessary to include one-coordinated O on surface sites. Such sites remain energetically favorable in the O-rich limit but quickly become unfavorable as we move into the O-poor regime. Similarly, edge and vertex sites on the nanoparticles lead to atoms being overall lower coordinated than they would be in either bulk or extended surfaces, even before the removal of any further O. The {001} and reconstructed {001} surfaces also exhibit vacancies that are favorable in the O-poor limit but, even if we were to unrealistically remove all of these O from a large Wulff construction particle, it would represent an extremely small value of δ compared to the value of δ observed in our model particles. We emphasize here that these are formation energies at 0 K with no consideration of the effects of configurational entropy of the nanoparticles and, while they provide evidence of a trend, we make no attempt to assign specific values of δ that would be expected at finite temperature.

We calculate the density of states (DOS) for the modeled nanoparticles and, to separate the properties due to the morphology of the nanoparticle and the properties due to reduction, we compare the DOS of the stoichiometric nanoparticles with the average DOS of all favorable reduced stoichiometries (Figure 5). The stoichiometric $Ti_{33}O_{33(2-\delta)}$

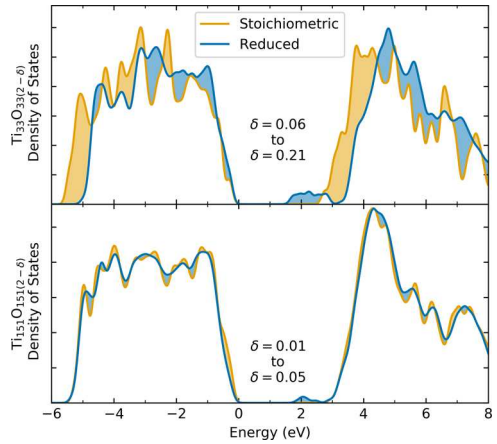

Figure 5. Density of states for (top) the $Ti_{33}O_{33(2-\delta)}$ particles and (bottom) the $Ti_{151}O_{151(2-\delta)}$ particles. Yellow represents the stoichiometric configuration and blue represents the average DOS of all favorable reduced configurations. The shaded regions indicate where a configuration has more states of a given energy. In the interest of clarity, the DOS represents the sum of both spin channels.

configuration has a band gap of around 0.3 eV lower than any of the $Ti_{151}O_{151(2-\delta)}$ configurations, which can be attributed to states at the top of the valence band associated with one-coordinated O sites. When considering reduced $Ti_{33}O_{33(2-\delta)}$ particles, these states are removed and the gap is increased to around 3.0 eV, comparable to the $Ti_{151}O_{151(2-\delta)}$. Reduced nanoparticles contain states in the band gap and, in the more highly reduced $Ti_{33}O_{33(2-\delta)}$ systems, these states appear deeper in the gap. For the $Ti_{151}O_{151(2-\delta)}$, the overall shape of the valence and conduction bands remains relatively unperturbed by reduction, but we see states appearing around 0.5−1.0 eV below the conduction band minimum (CBM) in the reduced case. In the case of the $Ti_{33}O_{33(2-\delta)}$ nanoparticles, reduction causes a large change in the shape of the bands. The gap states associated with reduced $Ti_{33}O_{33(2-\delta)}$ appear around 0.5−1.5 eV below the CBM, slightly deeper than the $Ti_{151}O_{151(2-\delta)}$ case. These results are consistent with observations that reduced anatase has increased photocatalytic performance.[84−86] Defect-free anatase requires ultraviolet radiation for photoexcitation, but these shallow states below the CBM would lead to increased visible light absorption, a very desirable trait if anatase is to be used as a photocatalyst under the sunlight. This increased absorption in the O-deficient anatase has been observed experimentally, and upon annealing in O-rich atmospheres, the states disappear, confirming that they originate from reduced Ti species.[87,88]

https://dx.doi.org/10.1021/acs.jpcc.0c06052
J. Phys. Chem. C 2020, 124, 23637−23647

To determine the behavior of excess charges, we perform Bader analysis on the model nanoparticles.[89−92] Unpaired spins would be visible to EPR, and so to facilitate comparison with the experiment, we also consider the absolute spin density associated with each site. In contrast to the extended models of bulk and of majority facets, we find that excess electrons present in the reduced nanoparticles have a tendency toward localizing to form Ti^{+3} species at undercoordinated Ti sites near surfaces (Figure 7), as evidenced by the high proportion of unpaired spins present compared to the number of excess electrons (Figure 6, top). To illustrate how the excess electrons

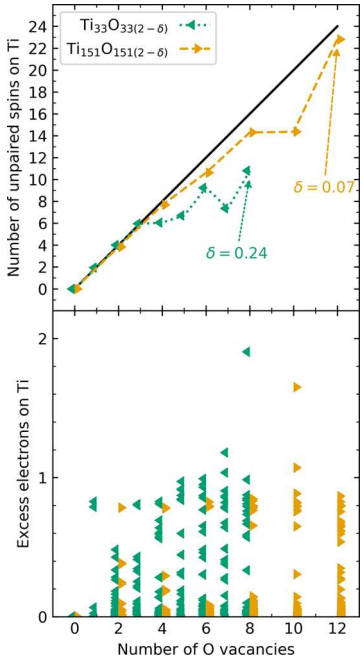

Figure 6. Plot of (top) the number of unpaired spins associated with Ti sites and (bottom) number of excess electrons associated with each Ti site against the number of O vacancies. The solid black line indicates the trend followed if the number of unpaired spins is equal to the number of excess electrons.

are distributed across sites, we determine how many gap-state electrons are associated with the Bader volumes of each Ti (Figure 6, bottom). For each stoichiometry of $Ti_{151}O_{151(2-\delta)}$ we determined to be stable, we see that in most cases the majority of the excess electrons are unpaired except for one stoichiometry that contains an anomalously low number of unpaired spins. Generally, there are two distinct bands that would correspond to Ti^{4+} and Ti^{3+}, except for the system containing a low number of unpaired spins (Figure 6, yellow points, 10 O vacancies). In this system, we see a particularly large number of excess electrons on one site, which would indicate that, rather than these excess electrons being delocalized, they have become trapped as a Ti^{2+} species, which would be a trap that is invisible to EPR. For the stable stoichiometries of $Ti_{33}O_{33(2-\delta)}$, we find that there is a comparatively lower proportion of unpaired spins than in the $Ti_{151}O_{151(2-\delta)}$ particles but we do not observe an increase in the number of sites with a number of electrons significant enough that they would correspond to a Ti^{2+}. Instead, we see far less distinct bands in the number of excess electrons and a far greater proportion of sites containing non-negligible numbers of excess electrons (Figure 6 and 7, bottom, green

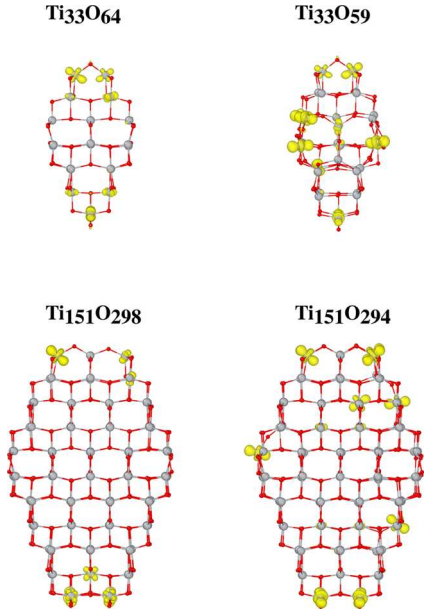

Figure 7. Absolute spin density isosurfaces (isosurface value 0.015 a_0^{-3}) for various stoichiometries of nanoparticle. Titanium and oxygen ions are represented by gray and red spheres, respectively.

points). This is indicative of two features: first, that the overall symmetry of the small particles is lower than that of the large particles, and second, the number of sites available to excess electrons is overall lower in the small particles, meaning that the traps associated with surface sites quickly begin to become filled, forcing more electrons into delocalized solutions.

These results lead us to predict that nanoparticle size has a pronounced effect on the degree to which a sample can be reduced, which, in turn, has a pronounced effect on the properties of the material due to the number of Ti^{3+} and Ti^{2+} species that are able to form. It has been observed that Ti^{3+} and Ti^{2+} states in highly reduced TiO_2 show extremely high photocatalytic activity.[5] We suggest that small nanoparticles would be better suited to photocatalytic applications for two reasons: first, that they would have a larger surface-area-to-volume ratio, which is beneficial in catalytic applications; and second, that smaller particles are easier to reduce, which would allow the creation Ti^{3+} and Ti^{2+} species and increase visible light activity, as discussed previously. We also predict that electron trapping would be more prevalent in nanocrystalline samples than in single crystals but, despite the majority of excess charges becoming trapped in our models, we do not predict that the majority of excess electrons would become trapped in samples containing larger nanoparticles. We remind the reader that our model nanoparticles are small and contain a disproportionate amount of surface features, whereas a larger nanoparticle would contain regions better described by the extended models of the bulk and surface and the delocalized configurations associated with such extended systems should be expected. Additionally, our results correspond to zero temperature, but it is expected that at finite temperature a proportion of these traps would become unstable; such behavior is reported in EPR studies where signals from Ti^{3+} species disappear at room temperature and in conductivity experiments where the conductivity of polycrystalline anatase increases with temperature.[93,94] One of these conductivity experiments[93] demonstrated higher conductivity in particles of smaller diameter, which would be in agreement with our

https://dx.doi.org/10.1021/acs.jpcc.0c06052
J. Phys. Chem. C 2020, 124, 23637−23647

prediction that these particles would be easier to reduce and would contain a higher number of carriers, but we emphasize that smaller particles would lead to lower electron mobility due to the number of trap states present in small, reduced particles. This concept is supported by the fact that, while increased conductivity is observed at decreased partial pressures of O_2 (i.e., in the O-poor limit, where vacancies are expected to be prevalent), it is also observed that conductivity saturates at high partial pressures of O_2,[94] which can be attributed to the decrease in free carrier concentration being balanced by an increase in electron mobility due to the smaller number of trap states present in less-reduced particles. We suggest that this trade-off between the number of carriers and electron mobility must be considered for applications where conductivity is important.

CONCLUSIONS

In summary, we have investigated oxygen vacancies and charge trapping in anatase through first-principles calculations of extended {101}, unreconstructed {001}, and reconstructed {001} surfaces and we compare these results to explicit models of $Ti_{33}O_{33(2-\delta)}$ and $Ti_{151}O_{151(2-\delta)}$ nanoparticles. We find that electrons introduced by vacancies at extended surfaces preferentially delocalize across all Ti sites. However, when considering $Ti_{33}O_{33(2-\delta)}$ and $Ti_{151}O_{151(2-\delta)}$ nanoparticles, electrons will localize to form Ti^{3+} species even when the level of reduction is relatively low and, when reduced further, Ti^{2+} species can also form. The presence of Ti^{3+} species associated with oxygen vacancies is frequently observed in EPR experiments on anatase nanoparticles,[27,53,85,86] but Ti^{2+} species represent a trap that would be invisible to EPR. The degree to which a particle can be reduced was found to depend strongly on the size of the particle, and we suggest that smaller particles will be preferable for photocatalytic applications due to providing better visible light absorption and increased surface area. For photovoltaic and battery applications, there will be a balance to be considered between the number of carriers introduced by vacancies and the number of trap states introduced due to particle size and number of under-coordinated Ti sites.

Our nanoparticle models show encouraging agreement with experimental observations, but there are still other open questions. For example, we have only considered an isolated Wulff construction nanoparticle but, depending on growth conditions, anatase nanoparticles can take a wide range of morphologies,[95,96] which may exhibit different size-dependent properties regarding reduction and charge trapping. Additionally, adsorption at the surface is important to photocatalytic processes and further investigation into how the presence of nanoparticle features such as edges and vertices changes the behavior of adsorbed species would be valuable. This study has provided insight into the reduction and the behavior of charges, but more work would be required to develop a full understanding of how the size and shape of nanoparticles affect their properties.

AUTHOR INFORMATION

Corresponding Author

James. A. Quirk − *Department of Physics, University of York, York YO10 5DD, U.K.*; orcid.org/0000-0003-3581-1615; Email: jaq502@york.ac.uk

Authors

Vlado K. Lazarov − *Department of Physics, University of York, York YO10 5DD, U.K.*

Keith P. McKenna − *Department of Physics, University of York, York YO10 5DD, U.K.*; orcid.org/0000-0003-0975-3626

Complete contact information is available at: https://pubs.acs.org/10.1021/acs.jpcc.0c06052

Notes

The authors declare no competing financial interest.

ACKNOWLEDGMENTS

K.P.M. and V.K.L. acknowledge support from EPSRC (EP/P006051/1) and K.P.M. from EPSRC (EP/P023843/1). This work made use of the facilities of Archer, the United Kingdom's National High-Performance Computing service, via our membership in the U.K. HPC Materials Chemistry Consortium, which is funded by EPSRC (EP/L000202/1 and EP/R029431/1). This project also made use of the Viking Cluster, which is a high-performance computation facility provided by the University of York. The authors are grateful for computational support from the University of York High-Performance Computing service, Viking, and the Research Computing team. All data created during this research are available by request from the University of York Research database at: https://doi.org/10.15124/971aeb5a-44d6-408c-b091-a5040ff18286.

REFERENCES

(1) Fujishima, A.; Honda, K. Electrochemical Photolysis of Water at a Semiconductor Electrode. *Nature* **1972**, *238*, 37.

(2) De Silva, N. L.; Jayasundera, A. C.; Folger, A.; Kasian, O.; Zhang, S.; Yan, C.-F.; Scheu, C.; Bandara, J. Superior Solar-to-Hydrogen Energy Conversion Efficiency by Visible Light-driven Hydrogen Production via Highly Reduced Ti^{2+}/Ti^{3+} States in a Blue Titanium Dioxide Photocatalyst. *Catal. Sci. Technol.* **2018**, *8*, 4657−4664.

(3) Kumar, S. G.; Devi, L. G. Review on Modified TiO_2 Photocatalysis Under UV/visible Light: Selected Results and Related Mechanisms on Interfacial Charge Carrier Transfer Dynamics. *J. Phys. Chem. A* **2011**, *115*, 13211−13241.

(4) Friedmann, D.; Mendive, C.; Bahnemann, D. TiO_2 for Water Treatment: Parameters Affecting the Kinetics and Mechanisms of Photocatalysis. *Appl. Catal., B* **2010**, *99*, 398−406.

(5) Dharmagunawardhane, D. S.; De Silva, N. L.; Gunatilake, U. B.; Yan, C.-F.; Bandara, J. Removal of Groundwater Nitrates by Heterogeneous Supramolecular Complexes-Like Photocatalytic System Based on In-Situ Generated and Highly Active Ti^{2+}/Ti^{3+} States in the Reduced TiO2. *Mol. Catal.* **2019**, *470*, 89−96.

(6) Wang, J.; Li, R.; Zhang, Z.; Sun, W.; Xie, Y.; Xu, R.; Xing, Z.; Zhang, X. Solar Photocatalytic Degradation of Dye Wastewater in the Presence of Heat-treated Anatase TiO_2 Powder. *Environ. Prog.* **2008**, *27*, 242−249.

(7) Scuderi, V.; Impellizzeri, G.; Romano, L.; Scuderi, M.; Brundo, M. V.; Bergum, K.; Zimbone, M.; Sanz, R.; Buccheri, M. A.; Simone, F.; et al. An Enhanced Photocatalytic Response of Nanometric TiO_2 Wrapping of Au Nanoparticles for Eco-friendly Water Applications. *Nanoscale* **2014**, *6*, 11189−11195.

(8) O'regan, B.; Grätzel, M. A Low-Cost, High-Efficiency Solar Cell Based on Dye-Sensitized Colloidal TiO_2 Films. *Nature* **1991**, *353*, 737.

(9) Bai, Y.; Mora-Sero, I.; De Angelis, F.; Bisquert, J.; Wang, P. Titanium Dioxide Nanomaterials for Photovoltaic Applications. *Chem. Rev.* **2014**, *114*, 10095−10130.

(10) Kim, H.-S.; Lee, J.-W.; Yantara, N.; Boix, P. P.; Kulkarni, S. A.; Mhaisalkar, S.; Grätzel, M.; Park, N.-G. High Efficiency Solid-State Sensitized Solar Cell-Based on Submicrometer Rutile TiO_2 Nanorod

and $CH_3NH_3PbI_3$ Perovskite Sensitizer. *Nano Lett.* **2013**, *13*, 2412−2417.
(11) Chen, J. S.; Tan, Y. L.; Li, C. M.; Cheah, Y. L.; Luan, D.; Madhavi, S.; Boey, F. Y. C.; Archer, L. A.; Lou, X. W. Constructing Hierarchical Spheres From Large Ultrathin Anatase TiO_2 Nanosheets With Nearly 100% Exposed (001) Facets for Fast Reversible Lithium Storage. *J. Am. Chem. Soc.* **2010**, *132*, 6124−6130.
(12) Kavan, L.; Grätzel, M.; Rathouskỳ, J.; Zukalb, A. Nanocrystalline TiO_2 (Anatase) Electrodes: Surface Morphology, Adsorption, and Electrochemical Properties. *J. Electrochem. Soc.* **1996**, *143*, 394.
(13) Myung, S.-T.; Kikuchi, M.; Yoon, C. S.; Yashiro, H.; Kim, S.-J.; Sun, Y.-K.; Scrosati, B. Black Anatase Titania Enabling Ultra High Cycling Rates for Rechargeable Lithium Batteries. *Energy Environ. Sci.* **2013**, *6*, 2609−2614.
(14) Xu, Y.; Lotfabad, E. M.; Wang, H.; Farbod, B.; Xu, Z.; Kohandehghan, A.; Mitlin, D. Nanocrystalline Anatase TiO_2: a New Anode Material for Rechargeable Sodium Ion Iatteries. *Chem. Commun.* **2013**, *49*, 8973−8975.
(15) Guo, Y.-G.; Hu, Y.-S.; Sigle, W.; Maier, J. Superior Electrode Performance of Nanostructured Mesoporous TiO_2 (Anatase) Through Efficient Hierarchical Mixed Conducting Networks. *Adv. Mater.* **2007**, *19*, 2087−2091.
(16) Ortiz, G. F.; Hanzu, I.; Djenizian, T.; Lavela, P.; Tirado, J. L.; Knauth, P. Alternative Li-Ion Battery Electrode Based on Self-Organized Titania Nanotubes. *Chem. Mater.* **2009**, *21*, 63−67.
(17) Deák, P.; Aradi, B.; Frauenheim, T. Quantitative Theory of the Oxygen Vacancy and Carrier Self-Trapping in Bulk TiO_2. *Phys. Rev. B* **2012**, *86*, No. 195206.
(18) Morgan, B. J.; Watson, G. W. A DFT+U Description of Oxygen Vacancies at the TiO_2 Rutile (110) Surface. *Surf. Sci.* **2007**, *601*, 5034−5041.
(19) Wallace, S. K.; Mckenna, K. P. Facet-Dependent Electron Trapping in TiO_2 Nanocrystals. *J. Phys. Chem. C* **2015**, *119*, 1913−1920.
(20) Wosiński, T. Evidence for the Electron Traps at Dislocations in GaAs Crystals. *J. Appl. Phys.* **1989**, *65*, 1566−1570.
(21) Maras, E.; Saito, M.; Inoue, K.; Jønsson, H.; Ikuhara, Y.; McKenna, K. P. Determination Of The Structure and Properties of an Edge Dislocation in Rutile TiO_2. *Acta Mater.* **2019**, *163*, 199−207.
(22) Stoneham, A.; Gavartin, J.; Shluger, A.; Kimmel, A.; Ramo, D. M.; Rønnow, H.; Aeppli, G.; Renner, C. Trapping, Self-Trapping and the Polaron Family. *J. Phys.: Condens. Matter* **2007**, *19*, No. 255208.
(23) Di Valentin, C. A Mechanism for the Hole-Mediated Water Photooxidation on TiO_2 (101) Surfaces. *J. Phys.: Condens. Matter* **2016**, *28*, No. 074002.
(24) Ohsawa, T.; Lyubinetsky, I. V.; Henderson, M. A.; Chambers, S. A. Hole-Mediated Photodecomposition of Trimethyl Acetate on a TiO_2 (001) Anatase Epitaxial Thin Film Surface. *J. Phys. Chem. C* **2008**, *112*, 20050−20056.
(25) Gribb, A. A.; Banfield, J. F. Particle Size Effects on Transformation Kinetics and Phase Stability in Nanocrystalline TiO_2. *Am. Miner.* **1997**, *82*, 717−728.
(26) Grätzel, M. Sol-Gel Processed TiO_2 Films for Photovoltaic Applications. *J. Sol-Gel Sci. Technol.* **2001**, *22*, 7−13.
(27) Berger, T.; Sterrer, M.; Diwald, O.; Knözinger, E.; Panayotov, D.; Thompson, T. L.; Yates, J. T. Light-Induced Charge Separation in Anatase TiO_2 Particles. *J. Phys. Chem. B* **2005**, *109*, 6061−6068.
(28) Sun, B.; Vorontsov, A. V.; Smirniotis, P. G. Role of Platinum Deposited on TiO_2 in Phenol Photocatalytic Oxidation. *Langmuir* **2003**, *19*, 3151−3156.
(29) Forro, L.; Chauvet, O.; Emin, D.; Zuppiroli, L.; Berger, H.; Levy, F. High Mobility n-type Charge Carriers in Large Single Crystals of Anatase (TiO2). *J. Appl. Phys.* **1994**, *75*, 633−635.
(30) Perdew, J. P.; Burke, K.; Ernzerhof, M. Generalized Gradient Approximation Made Simple. *Phys. Rev. Lett.* **1996**, *77*, 3865.
(31) Jensen, K. P.; Roos, B. O.; Ryde, U. Performance of Density Functionals for First Row Transition Metal Systems. *J. Chem. Phys.* **2007**, *126*, No. 014103.
(32) Tran, F.; Laskowski, R.; Blaha, P.; Schwarz, K. Performance on Molecules, Surfaces, and Solids of the Wu-Cohen GGA Exchange-Correlation Energy Functional. *Phys. Rev. B* **2007**, *75*, No. 115131.
(33) Zhang, Y.; Yang, W. A Challenge for Density Functionals: Self-Interaction Error Increases for Systems With a Noninteger Number of Electrons. *J. Chem. Phys.* **1998**, *109*, 2604−2608.
(34) Becke, A. D. A New Mixing of Hartree-Fock and Local Density-Functional Theories. *J. Chem. Phys.* **1993**, *98*, 1372−1377.
(35) Perdew, J. P.; Ernzerhof, M.; Burke, K. Rationale for Mixing Exact Exchange With Density Functional Approximations. *J. Chem. Phys.* **1996**, *105*, 9982−9985.
(36) Burke, K.; Ernzerhof, M.; Perdew, J. P. The Adiabatic Connection Method: a Non-Empirical Hybrid. *Chem. Phys. Lett.* **1997**, *265*, 115−120.
(37) Zhang, D.; Truhlar, D. G. Unmasking Static Correlation Error in Hybrid Kohn-Sham Density Functional Theory. *J. Chem. Theory Comput.* **2020**, *16*, 5432−5440.
(38) Deák, P.; Gali, A.; Sólyom, A.; Buruzs, A.; Frauenheim, T. Electronic Structure of Boron-Interstitial Clusters in Silicon. *J. Phys.: Condens. Matter* **2005**, *17*, S2141.
(39) Lyons, J.; Janotti, A.; Van de Walle, C. Carbon Impurities and the Yellow Luminescence in GaN. *Appl. Phys. Lett.* **2010**, *97*, No. 152108.
(40) Alkauskas, A.; Broqvist, P.; Pasquarello, A. Defect Levels Through Hybrid Density Functionals: Insights and Applications. *Phys. Status Solidi B* **2011**, *248*, 775−789.
(41) Di Paola, A.; Bellardita, M.; Palmisano, L. Brookite, the Least Known TiO_2 Photocatalyst. *Catalysts* **2013**, *3*, 36−73.
(42) Alkauskas, A.; Lyons, J. L.; Steiauf, D.; Van de Walle, C. G. First-Principles Calculations of Luminescence Spectrum Line Shapes for Defects in Semiconductors: the Example of GaN and ZnO. *Phys. Rev. Lett.* **2012**, *109*, No. 267401.
(43) Cui, Z.-H.; Wang, Y.-C.; Zhang, M.-Y.; Xu, X.; Jiang, H. Doubly Screened Hybrid Functional: an Accurate First-Principles Approach for Both Narrow- and Wide-gap Semiconductors. *J. Phys. Chem. Lett.* **2018**, *9*, 2338−2345.
(44) Skone, J. H.; Govoni, M.; Galli, G. Self-Consistent Hybrid Functional for Condensed Systems. *Phys. Rev. B* **2014**, *89*, No. 195112.
(45) Srebro, M.; Autschbach, J. Does a Molecule-Specific Density Functional Give an Accurate Electron Density? The Challenging Case of the CuCl Electric Field Gradient. *J. Phys. Chem. Lett.* **2012**, *3*, 576−581.
(46) Srebro, M.; Autschbach, J. Tuned Range-separated Time-Dependent Density Functional Theory Applied to Optical Rotation. *J. Chem. Theory Comput.* **2012**, *8*, 245−256.
(47) Kronik, L.; Stein, T.; Refaely-Abramson, S.; Baer, R. Excitation Gaps of Finite-Sized Systems From Optimally Tuned Range-Separated Hybrid Functionals. *J. Chem. Theory Comput.* **2012**, *8*, 1515−1531.
(48) Elmaslmane, A.; Wetherell, J.; Hodgson, M.; McKenna, K.; Godby, R. Accuracy of Electron Densities Obtained via Koopmans-Compliant Hybrid Functionals. *Phys. Rev. Mater.* **2018**, *2*, No. 040801.
(49) Vlček, V.; Eisenberg, H. R.; Steinle-Neumann, G.; Kronik, L.; Baer, R. Deviations From Piecewise Linearity in the Solid-State Limit With Approximate Density Functionals. *J. Chem. Phys.* **2015**, *142*, No. 034107.
(50) Spencer, J.; Alavi, A. Efficient Calculation of the Exact Exchange Energy in Periodic Systems Using a Truncated Coulomb Potential. *Phys. Rev. B* **2008**, *77*, No. 193110.
(51) Elmaslmane, A. R.; Watkins, M. B.; McKenna, K. P. First-Principles Modeling of Polaron Formation in TiO_2 Polymorphs. *J. Chem. Theory Comput.* **2018**, *14*, 3740−3751.
(52) Luo, Y.; Benali, A.; Shulenburger, L.; Krogel, J. T.; Heinonen, O.; Kent, P. R. Phase Stability of TiO_2 Polymorphs from Diffusion Quantum Monte Carlo. *New J. Phys.* **2016**, *18*, No. 113049.

https://dx.doi.org/10.1021/acs.jpcc.0c06052
J. Phys. Chem. C 2020, 124, 23637−23647

(53) Macdonald, I. R.; Howe, R. F.; Zhang, X.; Zhou, W. In Situ EPR Studies of Electron Trapping in a Nanocrystalline Rutile. *J. Photochem. Photobiol., A* **2010**, *216*, 238−243.
(54) Carey, J. J.; McKenna, K. P. Does Polaronic Self-Trapping Occur at Anatase TiO_2 Surfaces. *J. Phys. Chem. C* **2018**, *122*, 27540−27553.
(55) Quirk, J. A.; Lazarov, V. K.; McKenna, K. P. Electronic Properties of {112} and {110} Twin Boundaries in Anatase TiO_2. *Adv. Theory Simul.* **2019**, *2*, No. 1900157.
(56) Elmaslmane, A. R. Localised Electronic States in Model Systems and Semiconductors. Ph.D. Thesis, University of York, 2019.
(57) Liu, J.; Liu, Q.; Fang, P.; Pan, C.; Xiao, W. First Principles Study of the Adsorption of a NO Molecule on N-doped Anatase Nanoparticles. *Appl. Surf. Sci.* **2012**, *258*, 8312−8318.
(58) Lei, Y.; Liu, H.; Xiao, W. First Principles Study of the Size Effect of TiO_2 Anatase Nanoparticles in Dye-Sensitized Solar Cell. *Modell. Simul. Mater. Sci. Eng.* **2010**, *18*, No. 025004.
(59) De Angelis, F.; Fantacci, S.; Selloni, A. Alignment of the Dye's Molecular Levels with the TiO_2 Band Edges in Dye-sensitized Solar Cells: a DFT-TDDFT study. *Nanotechnology* **2008**, *19*, No. 424002.
(60) Valero, R.; Morales-Garcia, A.; Illas, F. Investigating the Character of Excited States in TiO2 Nanoparticles from Topological Descriptors: Implications for Photocatalysis. *Phys. Chem. Chem. Phys.* **2020**, *22*, 3017−3029.
(61) Lamiel-Garcia, O.; Ko, K. C.; Lee, J. Y.; Bromley, S. T.; Illas, F. When Anatase Nanoparticles Become Bulklike: Properties of Realistic TiO_2 Nanoparticles in the 1-6 nm Size Range From All Electron Relativistic Density Functional Theory Based Calculations. *J. Chem. Theory Comput.* **2017**, *13*, 1785−1793.
(62) Morales-García, Á.; Valero, R.; Illas, F. Electronic Properties of Realistic Anatase TiO_2 Nanoparticles from G_0W_0 Calculations on a Gaussian and Plane Waves Scheme. *J. Chem. Theory Comput.* **2019**, *15*, 5024−5030.
(63) Lamiel-Garcia, O.; Cuko, A.; Calatayud, M.; Illas, F.; Bromley, S. T. Predicting Size-Dependent Emergence of Crystallinity in Nanomaterials: Titania Nanoclusters Versus Nanocrystals. *Nanoscale* **2017**, *9*, 1049−1058.
(64) Morales-García, Á.; Lamiel-García, O.; Valero, R.; Illas, F. Properties of Single Oxygen Vacancies on a Realistic $(TiO_2)_{84}$ Nanoparticle: a Challenge for Density Functionals. *J. Phys. Chem. C* **2018**, *122*, 2413−2421.
(65) Ko, K. C.; Lamiel-García, O.; Lee, J. Y.; Illas, F. Performance of a Modified Hybrid Functional in the Simultaneous Description of Stoichiometric and Reduced TiO_2 Polymorphs. *Phys. Chem. Chem. Phys.* **2016**, *18*, 12357−12367.
(66) Perdew, J. P.; Parr, R. G.; Levy, M.; Balduz, J. L., Jr. Density-Functional Theory for Fractional Particle Number: Derivative Discontinuities of the Energy. *Phys. Rev. Lett.* **1982**, *49*, No. 1691.
(67) Levy, M.; Perdew, J. P.; Sahni, V. Exact Differential Equation for the Density and Ionization Energy of a Many-Particle System. *Phys. Rev. A* **1984**, *30*, No. 2745.
(68) Perdew, J. P.; Levy, M. Comment on "Significance of the Highest Occupied Kohn-Sham Eigenvalue". *Phys. Rev. B* **1997**, *56*, No. 16021.
(69) VandeVondele, J.; Krack, M.; Mohamed, F.; Parrinello, M.; Chassaing, T.; Hutter, J. Quickstep: Fast and Accurate Density Functional Calculations Using a Mixed Gaussian and Plane Waves Approach. *Comput. Phys. Commun.* **2005**, *167*, 103−128.
(70) Guidon, M.; Hutter, J.; VandeVondele, J. Robust Periodic Hartree-Fock Exchange for Large-Scale Simulations Using Gaussian Basis Sets. *J. Chem. Theory Comput.* **2009**, *5*, 3010−3021.
(71) Guidon, M.; Hutter, J.; VandeVondele, J. Auxiliary Density Matrix Methods for Hartree-Fock Exchange Calculations. *J. Chem. Theory Comput.* **2010**, *6*, 2348−2364.
(72) VandeVondele, J.; Hutter, J. Gaussian Basis Sets for Accurate Calculations on Molecular Systems in Gas and Condensed Phases. *J. Chem. Phys.* **2007**, *127*, No. 114105.
(73) Krack, M. Pseudopotentials for H to Kr Optimized for Gradient-Corrected Exchange-Correlation Functionals. *Theor. Chem. Acc.* **2005**, *114*, 145−152.
(74) Goedecker, S.; Teter, M.; Hutter, J. Separable Dual-space Gaussian Pseudopotentials. *Phys. Rev. B* **1996**, *54*, No. 1703.
(75) Hartwigsen, C.; Gœdecker, S.; Hutter, J. Relativistic Separable Dual-Space Gaussian Pseudopotentials From H to Rn. *Phys. Rev. B* **1998**, *58*, No. 3641.
(76) Rahm, J.; Erhart, P. WulffPack: A Python Package for Wulff Constructions. *J. Open Source Softw.* **2020**, *5*, No. 1944.
(77) Martyna, G. J.; Tuckerman, M. E. A Reciprocal Space Based Method for Treating Long Range Interactions in Ab Initio and Force-Field-Based Calculations in Clusters. *J. Chem. Phys.* **1999**, *110*, 2810−2821.
(78) Lazzeri, M.; Selloni, A. Stress-Driven Reconstruction of an Oxide Surface: the Anatase TiO_2 (001)-(1× 4) Surface. *Phys. Rev. Lett.* **2001**, *87*, No. 266105.
(79) Liang, Y.; Gan, S.; Chambers, S. A.; Altman, E. I. Surface Structure of Anatase TiO_2 (001): Reconstruction, Atomic Steps, and Domains. *Phys. Rev. B* **2001**, *63*, No. 235402.
(80) Lee, H.-Y.; Clark, S. J.; Robertson, J.; et al. Calculation of Point Defects in Rutile TiO_2 by the Screened-exchange Hybrid Functional. *Phys. Rev. B* **2012**, *86*, No. 075209.
(81) Na-Phattalung, S.; Smith, M. F.; Kim, K.; Du, M.-H.; Wei, S.-H.; Zhang, S.; Limpijumnong, S. First-Principles Study of Native Defects in Anatase TiO_2. *Phys. Rev. B* **2006**, *73*, No. 125205.
(82) He, Y.; Dulub, O.; Cheng, H.; Selloni, A.; Diebold, U. Evidence for the Predominance of Subsurface Defects on Reduced Anatase TiO_2 (101). *Phys. Rev. Lett.* **2009**, *102*, No. 106105.
(83) Scheiber, P.; Fidler, M.; Dulub, O.; Schmid, M.; Diebold, U.; Hou, W.; Aschauer, U.; Selloni, A. (Sub) Surface Mobility of Oxygen Vacancies at the TiO_2 Anatase (101) Surface. *Phys. Rev. Lett.* **2012**, *109*, No. 136103.
(84) Justicia, I.; Ordejón, P.; Canto, G.; Mozos, J. L.; Fraxedas, J.; Battiston, G. A.; Gerbasi, R.; Figueras, A. Designed Self-Doped Titanium Oxide Thin Films for Efficient Visible-Light Photocatalysis. *Adv. Mater.* **2002**, *14*, 1399−1402.
(85) Liu, X.; Xu, H.; Grabstanowicz, L. R.; Gao, S.; Lou, Z.; Wang, W.; Dai, Y.; Xu, T.; et al. Ti^{3+} Self-doped TiO_{2-x} Anatase Nanoparticles via Oxidation of TiH_2 in H_2O_2. *Catal. Today* **2014**, *225*, 80−89.
(86) Wei, S.; Ni, S.; Xu, X. A New Approach to Inducing Ti^{3+} in Anatase TiO_2 for Efficient Photocatalytic Hydrogen Production. *Chin. J. Catal.* **2018**, *39*, 510−516.
(87) Sekiya, T.; Kamei, S.; Kurita, S. Luminescence of Anatase TiO_2 Single Crystals Annealed in Oxygen Atmosphere. *J. Lumin.* **2000**, *87-89*, 1140−1142.
(88) Choudhury, B.; Choudhury, A. Oxygen Defect Dependent Variation of Band Gap, Urbach Energy and Luminescence Property of Anatase, Anatase-Rutile Mixed Phase and of Rutile Phases of TiO_2 Nanoparticles. *Physica E* **2014**, *56*, 364−371.
(89) Tang, W.; Sanville, E.; Henkelman, G. A Grid-Based Bader Analysis Algorithm Without Lattice Bias. *J. Phys.: Condens. Matter* **2009**, *21*, No. 084204.
(90) Sanville, E.; Kenny, S. D.; Smith, R.; Henkelman, G. Improved Grid-Based Algorithm for Bader Charge Allocation. *J. Comput. Chem.* **2007**, *28*, 899−908.
(91) Henkelman, G.; Arnaldsson, A.; Jónsson, H. A Fast and Robust Algorithm for Bader Decomposition of Charge Density. *Comput. Mater. Sci.* **2006**, *36*, 354−360.
(92) Yu, M.; Trinkle, D. R. Accurate and Efficient Algorithm for Bader Charge Integration. *J. Chem. Phys.* **2011**, *134*, No. 064111.
(93) Huber, B.; Brodyanski, A.; Scheib, M.; Orendorz, A.; Ziegler, C.; Gnaser, H. Nanocrystalline Anatase TiO_2 Thin Films: Preparation and Crystallite Size-Dependent Properties. *Thin Solid Films* **2005**, *472*, 114−124.
(94) Dittrich, T.; Weidmann, J.; Koch, F.; Uhlendorf, I.; Lauermann, I. Temperature-and Oxygen Partial Pressure-Dependent Electrical

https://dx.doi.org/10.1021/acs.jpcc.0c06052
J. Phys. Chem. C 2020, 124, 23637−23647

Conductivity in Nanoporous Rutile and Anatase. *Appl. Phys. Lett.* **1999**, *75*, 3980−3982.
(95) Sellschopp, K.; Heckel, W.; Gäding, J.; Schröter, C. J.; Hensel, A.; Vossmeyer, T.; Weller, H.; Müller, S.; Vonbun-Feldbauer, G. Shape-Controlling Effects of Hydrohalic and Carboxylic Acids in TiO_2 Nanoparticle Synthesis. *J. Chem. Phys.* **2020**, *152*, No. 064702.
(96) Liu, G.; Jimmy, C. Y.; Lu, G. Q. M.; Cheng, H.-M. Crystal Facet Engineering of Semiconductor Photocatalysts: Motivations, Advances and Unique Properties. *Chem. Commun.* **2011**, *47*, 6763−6783.

https://dx.doi.org/10.1021/acs.jpcc.0c06052
J. Phys. Chem. C 2020, 124, 23637−23647